A Computational Comparison Between Pomotrelvir and Nirmatrelvir Binding and Reactivity with SARS-CoV-2 Main Protease. Implications for Resistance Mechanisms.

Johanna Schillings,[a] Carlos A. Ramos-Guzmán,[ab]* J. Javier Ruiz-Pernía[a] and Iñaki Tuñón[a]*

[a]Departamento de Química Física, Universitat de València, 46100 Burjassot (Spain)
[b]Instituto de Materiales Avanzados, Universidad Jaume I, 12071 Castelló (Spain)

*to whom correspondence should be addressed
ignacio.tunon@uv.es
carlos.a.ramos@uv.es

Abstract

This study investigates the binding mode and reaction mechanism between pomotrelvir and the SARS-CoV-2 main protease using a combination of molecular mechanics and hybrid quantum mechanics / molecular mechanics simulations. Alchemical transformations where each Pi group of pomotrelvir was transformed into its counterpart in nirmatrelvir were performed to unravel the individual contribution of each group of the inhibitor to the binding and reaction processes. We have shown that while a γ-lactam ring is preferred at position P1, a δ-lactam ring could be an alternative to be incorporated at this position in the design of inhibitors designed against wild-type main protease and for variants presenting mutations at position 166. For the P2 position, tertiary amines are clearly preferred with respect to secondary amines, because the ability to act as a hydrogen bond donor seem to favour more the interaction with the solvent than with the protein, decreasing the affinity for the enzyme. In addition, flexible groups at P2 position disfavour the formation of the covalent complex because they can disrupt the preorganization of the active site, favouring the exploration of non-reactive conformations. The substitution of the P2 group of pomotrelvir by that of nirmatrelvir resulted in a compound, here named as C2, that presents a notable improvement in the binding energy and a higher population of reactive conformations in the Michaelis complex. Analysis of the chemical reaction to form the covalent complex has shown a similar reaction mechanism and activation free energies for pomotrelvir, nirmatrelvir and C2. We hope that these findings could be useful to design better inhibitors to fight present and future variants of SARS-CoV-2 virus.

1. Introduction

There are two possible strategies to fight COVID-19, the disease caused by SARS-CoV-2 virus: the use of vaccines and antivirals.[1,2] These two strategies are threatened by the variability and continuous adaptation of the virus, which makes continuous research necessary for the improvement of both.[3] Resistance mechanisms to the use of nirmatrelvir, the active principle of Paxlovid, a FDA approved antiviral drug developed by Pfizer, have been already reported.[4] Nirmatrelvir is a covalent inhibitor of the SARS-CoV-2 main protease (or 3CL protease). This enzyme is a cysteine protease playing an essential role in the replication cycle of the virus, performing most of the cleavage events on the pp1a and pp1bab polyproteins produced post RNA translation. Cleavage of the polyproteins results in the formation of functional non-structural proteins needed by the virus during its replication cycle.

One of the advantages of nirmatrelvir is that it can be administered orally, facilitating the treatment of COVID-19 patients. However, certain mutations observed in variants of the main protease increase the virus resistance to treatments with nirmatrelvir by reducing the affinity between the drug and the enzyme and thereby decreasing the efficiency of the treatment.[5–7] This has stimulated the search of new drugs targeting this protease with the aspiration to develop an arsenal of possibilities to fight different variants that may appear with the clinical use of current antivirals. Pomotrelvir is a covalent inhibitor of the SARS-CoV-2 main protease recently developed by Pardes Biosciences[8] presenting the same nitrile warhead as nirmatrelvir (see Figure 1). Once in the active site these drugs react with the catalytic cysteine forming a thioimidate adduct. The reaction mechanism involves the activation of the catalytic dyad by a proton transfer from Cys145 to His41, forming an ion pair (IP). After this activation, the reaction proceeds through a water-mediated proton transfer from His41 to the nitrogen atom on the nitrile group, concerted with the nucleophilic attack of the Sγ atom of Cys145 to the electrophilic carbon on the nitrile group.[9] Nirmaltrelvir and pomotrelvir differ in the substituents appearing after the warhead, denoted as Pi, which are designed to fit into the corresponding Si subsites of the enzymatic active site. In nirmatrelvir P1 group is a γ-lactam ring, while in pomotrelvir is a δ-lactam ring. The presence of a lactam ring in this position is a common feature seen in most inhibitors of SARS-CoV and SARS-CoV-2 main proteases, exploiting the requirement for a glutamine residue just before the cleavage site in these enzymes.[10] Both drugs present hydrophobic groups at the P2 position, inspired by the preference shown by this protease for a leucine residue placed in the same position in its natural substrate. A gem-dimethylcyclopropylproline is used in nirmatrelvir, while a cyclopropylmethyl group is found in pomotrelvir. Recent studies show that the nature of the P2 group can have an important impact on the inhibitory potency of nitrile-based compounds.[11] Finally, nirmatrelvir features two chemical groups in its P3 and P4 positions while pomotrelvir has a larger, more conformational restricted, group at its P3 position. In general, the specificity for these positions is lower, although the chemical nature of these groups may affect the stability of the compounds.[9,11,12]
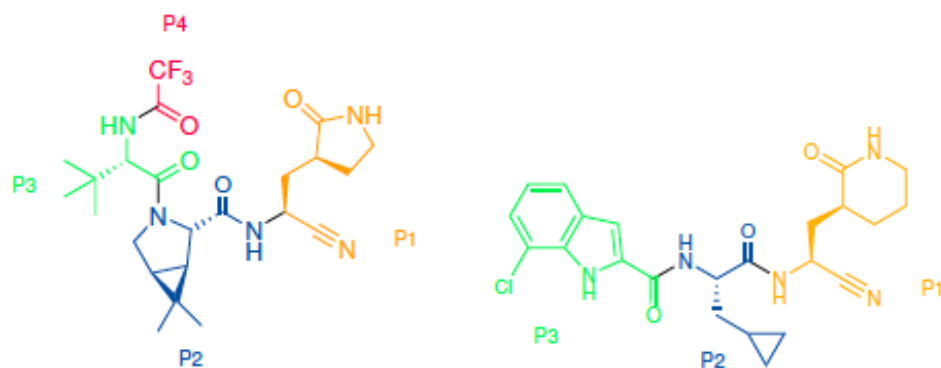
Figure 1. *Comparison between the chemical structures of nirmatrelvir (left) and pomotrelvir (right)*

The similarities and differences between these two drugs offer the opportunity to analyse, from a computational point of view, the role of the different P*i* groups during the binding process of the inhibitor (I) into the active site of the enzyme (E) to form the noncovalent enzyme inhibitor complex (EI) and during the reaction that results in the formation of a covalent complex (E-I):

$$E + I \underset{k_{-1}}{\overset{k_1}{\rightleftharpoons}} EI \overset{k_2}{\rightarrow} E - I$$
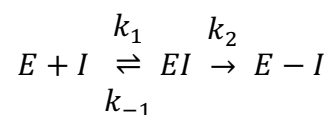
A comparative analysis between these two drugs can reveal the role of the different groups and the advantages/disadvantages of each choice. In this regard, it is interesting to note that, despite the promising results reached by pomotrelvir in the phase 1 of its clinical trials, Pardes Biosciences recently decided to halt its development after the results from its phase 2 trials because the drug was not as effective enough in reducing the viral load in patients.[13] This underscores the necessity to conduct further research on the design of new compounds, with the goal of not only improving inhibitory properties towards SARS-CoV-2 main protease but also enhancing its pharmacokinetic properties.

In the present study, we used a combination of Molecular Dynamics (MD) simulations, alchemical transformations and hybrid Quantum Mechanics / Molecular Mechanics (QM/MM) free energy calculations to investigate the inhibitory activity of pomotrelvir and several derivatives, where the impact of different P*i* groups has been evaluated. Specifically, our results focus on the role of the P2 group, highlighting some principles that can be used to improve the design of future drug candidates targeting SARS-CoV-2 main protease.

2. Methodology

2.1. Classical Molecular Dynamics Simulations.

The pomotrelvir inhibitor was broken down into three distinct residues (see **Figure 1**, right) and each of these were parameterized separately following the nonstandard residue parameterization procedure, using the Antechamber program[14] from AmberTools[15] package. The atomic charges were obtained with the restrained electrostatic potential (RESP) method[16] at the HF/6-31G* level. The tool tLeap from AmberTools[15] was applied to build the system using the forcefield ff14SB[17] to describe the canonical amino acids. The parameters for each parameterized residue used in this study can be found in the supplementary information material.

The Michaelis complex (MC) of the SARS-CoV-2 main protease and pomotrelvir was built using as template a pre-existing complex structure formed between the SARS-CoV-2 main protease and the inhibitor PF-00835231. This structure was obtained from the Protein Data Bank (PDB),[18] with the accession code 6XHM.[19] Missing atoms were added later during the system building process with tLeap using the parameters previously obtained. The most probable protonation state of every residue of the MC complex at pH 7.4 was determined using PROPKA3.0.[20] A total of 8 Na^+ ions were added to neutralize the charge of the system. The protein-inhibitor complex was solvated using TIP3P water molecules, ensuring a minimum distance of 12 Å between the atoms of the MC and the boundaries of the solvation box. To relax the built system, 500 steps of the steepest descent method were performed followed by the conjugate gradient method until the root mean square of the gradient was below 10^{-3} kcal·mol^{-1}·Å^{-1}. Using a linear heating ramp the temperature of the system was increased from 0 to 300 K for 120 ps followed by a 20 ps simulation at 300 K. Throughout this period, the positions of the heavy atoms of the backbone were restrained using a harmonic potential with a force constant of 20 kcal·mol^{-1}·Å^{-2}. Next, the system was equilibrated within the NPT ensemble (300 K and 1 bar) during 7.5 ns. During this equilibration, the force constants for the restraints of the heavy atoms were reduced from 15 to 3 kcal·mol^{-1}·Å^{-2}, lowering it in steps of 3 units every 1.25 ns, ending with a restraint free simulation of 1.25 ns. To ensure sufficient sampling, three replicas of 1 μs each were run in the NVT ensemble at 300 K. Within these simulations, a time step of 2 fs was used, employing SHAKE[21] to constrain bonds involving hydrogen atoms. Long-range electrostatic interactions were described using the particle mesh Ewald method[22,23] while the cut-off radius to evaluate the short-range interactions was 10 Å. The Berendsen barostat and the Langevin thermostat were used to control pressure and temperature, respectively. The GPU version of PMEMD[24,25] was employed for all classical molecular dynamics simulations. The same procedure was followed to simulate the complex of SARS-CoV-2 main protease with the nirmatrelvir[9] and the chimeric structures C2 and C2' proposed in this work.

2.2.   *QM/MM Calculations*

To obtain the free-energy profile associated with the inhibition mechanism, the adaptive string method (ASM)[26] developed in our group was used. By employing ASM, we localize the minimal free-energy pathway (MFEP) within a multidimensional free-energy surface. The reaction mechanism was explored by employing 96 replicas of the system, represented as string nodes, to establish connections between the reactant and product regions along the MFEP in a multidimensional space defined by the seven collective variables (CVs) defined in **Figure 2**. At the beginning, an initial guess for the chemical reaction is proposed. Then, by running QM/MM MD simulations, the nodes evolve towards their lowest free-energy gradient and are evenly redistributed along the string, preventing them from settling into the global minima. This process is repeated until the string converges to the MFEP as determined by the Root Mean Square Deviation (RMSD) of the CVs that must drop below 0.1 amu$^{1/2}$·Å for a minimum duration of 2 ps. Every 50 steps, replica exchange between consecutive string nodes was attempted to ensure an adequate sampling. Upon achieving convergence, a path-CV, referred as s, is established to quantify the progression of the system along the MFEP from reactants to products.[27] This path-CV is utilized as the reaction coordinate to trace the free energy profile associated with the chemical reaction. At this stage each node underwent QM/MM simulations lasting 10 ps, and the integration was done using the weighted histogram analysis method (WHAM).[28] In order to maintain a probability density distribution of the reaction coordinate as uniform as possible, the force constants used to bias the ASM simulations were determined on-the-fly.[26] As the total length of the reaction coordinate s could be different for each system we present the results as a function of a renormalized reaction coordinate ($RC = \frac{s - s_{min}}{s_{max} - s_{min}}$) that takes values between 0 and 1 in all the cases. This is made in order to be able to compare several inhibitors properly.

The QM region (see **Figure 2**) was described with the B3LYP functional[29,30], using the 6-31+G* basis set and D3 dispersion corrections.[31] In the context of mechanistic investigations, the QM region encompassed the side chains of the catalytic dyad (His41 and Cys145), the water molecule participating in the reaction mechanism, and the warhead and backbone atoms of residues P1 and P2 within the pomotrelvir inhibitor. All remaining atoms were treated at the MM level, as detailed in the classical molecular dynamics section. This selection proves to be highly suitable for characterizing the acylation of the SARS-CoV-2 main protease with a peptide substrate[32] and with some inhibitors,[9,19,33,34] yielding activation free energies in excellent agreement with experimental data. Furthermore, a comprehensive investigation into the proton transfer between cysteine and histidine indicated that the B3LYP functional is the most appropriate choice to described this step.[35] The QM/MM calculations were carried out utilizing a modified version of Amber18[15,36] coupled to Gaussian16[37] for density functional theory calculations. A cutoff radius of 15 Å was applied to all the QM/MM interactions. The integration time step employed in the QM/MM simulations was set to 1 fs and the mass of the transferred hydrogen atoms was set equal to 2 amu.
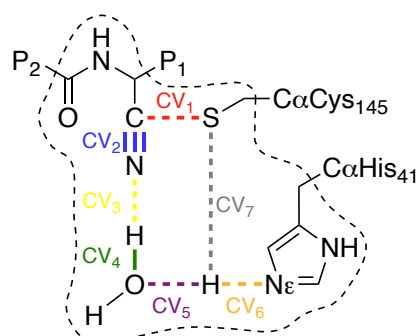
Figure 2. *Illustration of the CVs and QM region employed to describe the inhibition reaction mechanism.*

2.3. Alchemical Transformations

We employed the Amber Thermodynamic Integration (TI) protocol, as reported by He et al,[38] to assess the alterations in binding free energy during the formation of the noncovalent complex (EI) associated with modifications in ligands ($\Delta\Delta G_{bind}$). The $\Delta\Delta G_{bind}$ values were determined by computing the difference between the average values of five replicas for each transformation in aqueous solution and within the protein environment. Transformations were defined through a coupling parameter, λ, changing from 0 to 1. The initial configuration for each of the five transformations was equilibrated at a λ value of 0.5. In each replica, 9 λ values were simulated (0.01592, 0.08198, 0.19331, 0.33787, 0.5, 0.66213, 0.80669, 0.91802, and 0.98408) during 5 ns. The configuration obtained after 3.0 ns of simulation at λ 0.5 was used as the initial configuration for both the preceding and the subsequent λ values in the series. This process was repeated until the first and last λ values were simulated. TI was performed using only the final 4 ns of each λ simulation with the gaussian quadrature integration method. The binding free energy was determined by calculating the difference between the averaged values for the transformation occurring in the enzymatic active site and that taking place in aqueous solution.

3. Results

3.1. Non-covalent complex

The Michaelis complex model between the SARS-CoV-2 main protease and pomotrelvir demonstrated high stability across the three replicas of 1 μs. As Figure S1 illustrates, minor fluctuations for the RMSD of the inhibitor and protein atoms can be observed. The P1 group fits into a subpocket, S1, which is formed by residues Phe140, Leu141, Ser144, Glu166, His172, and Ser2 of protomer B (henceforth referred to as Ser1'); the P2 cyclopropylmethyl group establishes non-polar interactions with His41, His164, Met165 and Asp187 while the amino backbone group is hydrogen bonded to Gln189 side chain. The P3 group is largely exposed to the solvent, but it also displays a hydrogen bond interaction to the backbone of Glu166, and a non-polar contact with Met165.

The hydrogen bond pattern established by pomotrelvir in the active site of SARS-CoV-2 main protease can be compared to that obtained for nirmatrelvir inhibitor with the same enzyme[9] (see Figure 3a). The hydrogen bond patterns are almost identical for both inhibitors, although subtle differences were spotted. One of the differences is a decrease in the strength of interactions observed between the P1 group of pomotrelvir and Glu166, as compared to the interactions formed by nirmatrelvir with the same residue. This variation is likely attributed to the bulkier nature of the δ-lactam ring of pomotrelvir compared to the γ-lactam ring of nirmatrelvir. The carboxylate side chain (Cδ atom) group of Glu166 is found at an average distance of 3.65 ± 0.31 Å from the NH group of the γ-lactam ring in nirmatrelvir, while this distance increases to 3.96 ± 0.41 Å in the case of pomotrelvir (see **Figure 3** and S2). This change in the interaction of the P1 group between nirmatrelvir and pomotrelvir could be an advantage for the use of the latter to fight the coronavirus variants presenting the E166V mutation in the main protease. As recently reported, this kind of mutations make the virus resistant to nirmatrelvir.[6] An inhibitor with a δ-lactam substituent at P1 could be a better option to bind to the E166V main protease mutant, because the resulting complex would not be as dependent on the interaction with the side chain of residue 166 as in the case of the inhibitor presenting a γ-lactam ring at the same position.

One striking difference between both inhibitors is tied to a key structural variation between the P2 groups in nirmatrelvir and pomotrelvir. The later presents a cyclopropylmethyl group as side chain in this position while the mainchain amino group is a secondary amine that can act as a hydrogen bond donor with the carbonyl oxygen atom of Gln189. Instead, nirmatrelvir includes a gem-dimethylcyclopropylproline group at P2, which transforms the mainchain amino group into a tertiary amine unable to act as hydrogen bond donor. This structural change between the inhibitors results in a weaker interaction of the P2 group of nirmatrelvir with Gln189 compared to pomotrelvir, as observed in **Figure 3**a and Figure S2. It must be noticed, as will be discussed below, that this additional protein-inhibitor hydrogen bond interaction does not necessarily translates into an improved binding energy because, in that case, one also has to consider the interaction of the inhibitor with the solvent.

Finally, the P3 group of pomotrelvir is a rigid 7-chloroindole-2-carbonyl group, while in nirmatrelvir there are two groups: *tert*-leucine, P3, and trifluoroacetyl, P4. The two inhibitors stablish a similar interaction pattern with Glu166 backbone atoms as show in **Figure 3**b and **Figure 3**c, being the interaction slightly tighter in the case of pomotrelvir, as (see Figure S2), which could be related to the reduced flexibility of its P3 group.
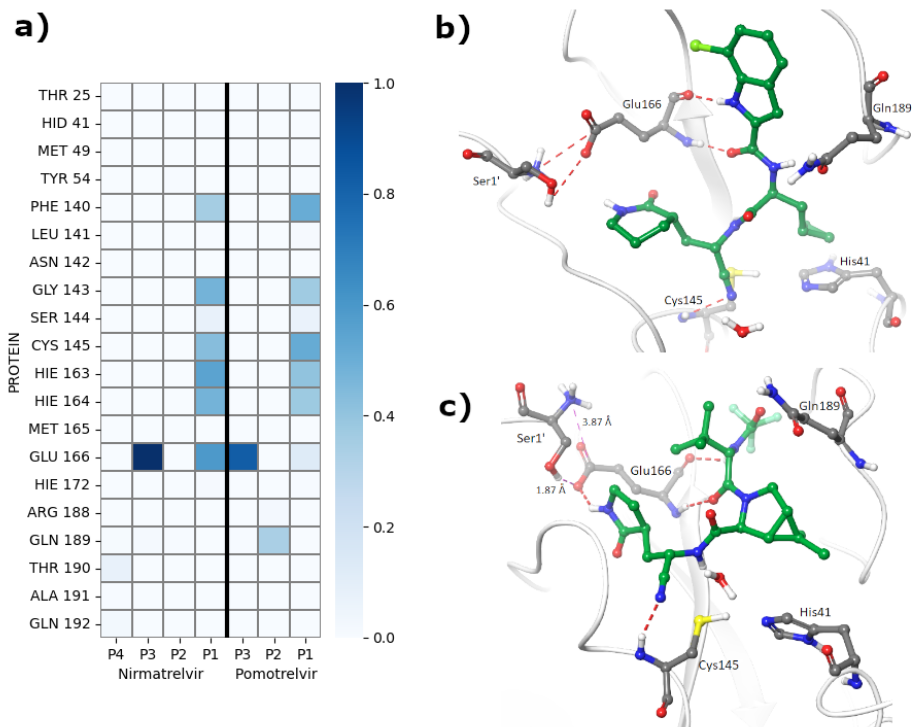
Figure 3. *Michaelis Complex formed between pomotrelvir and nirmatrelvir with the SARS-CoV-2 main protease. a) Frequency of protein-inhibitor hydrogen bond interactions. The colour intensity corresponds to the observed frequency between inhibitors Pi groups and residues of the main protease during MD simulations, b) binding pose of pomotrelvir, c) binding pose of nirmatrelvir.*

The structural differences between both inhibitors also have consequences on the preorganization of the active site. In the left panel of **Figure 4**, it is shown the distributions of distances between the proton donor and acceptor atoms in the catalytic dyad, Cys145 and His41. As said before, the proton transfer from cysteine to histidine is the first step that activates the enzyme for covalent inhibition. It can be observed that the catalytic dyad is better positioned for a proton transfer from Cys145 to His41 with nirmatrelvir, orange curve, than with pomotrelvir, blue curve. Likewise, the right panel in **Figure 4** indicates a closer positioning of Cys145 with respect to the inhibitor warhead to perform the nucleophilic attack in nirmatrelvir than in pomotrelvir.
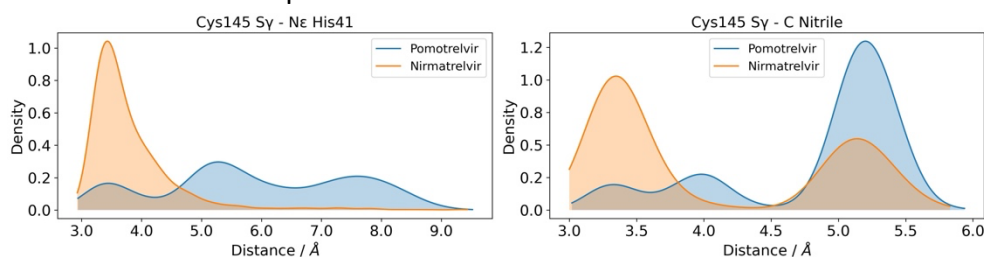

Figure 4. *Distribution function of the Cys145 Sγ atom relative to the His41 Nε atom (left) and to the carbon atom in the nitrile group (right).*

These differences can be attributed to the behaviour of the P2 side chain group of pomotrelvir. Figure S3 illustrates that this group is flexible in the active site and when it rotates around the Cα-Cβ bond induces a conformational change in the surroundings. Figure S3 shows the disruption of the hydrogen bond interaction between the mainchain nitrogen atom in Gln189 and the oxygen atom in Met49 occurring after P2 group rotation. Breaking the Gln189-Met49 hydrogen bond leads to a separation of the regions defined by residues Ile43 to Leu67 in domain I and Val186 and Ala191 in domain II (see Figure S4) opening the active site and increasing the distance between the catalytic dyad. Our MD simulations show that even upon the return of the P2 side chain group to its initial position both hydrogen bond interactions struggle to be re-established. Thus, the binding of pomotrelvir could alter the preorganization of the active site needed for the covalent reaction between the inhibitor and the enzyme, decreasing then its inhibitory efficiency.

3.2.   Alchemical Transformations

Observing the differences in the binding modes of pomotrelvir and nirmatrelvir on the active site of the SARS-CoV-2 main protease, we investigated the impact of P*i* groups on the binding energies of both inhibitors, as an attempt to discern which design could lead to a better affinity with the main protease. To achieve this, alchemical transformations were performed to create a series of chimeric structures, named C1, C2 and C3, where each of the P*i* groups of pomotrelvir was substituted by the equivalent group in nirmatrelvir. In addition, because of the central role of the P2 group, we also considered the substitution of this group in pomotrelvir by the P2 group from UAWJ9-36-1, a compound with potent binding and enzymatic inhibition against SARS-CoV-2 main protease,[39] and named the resulting structure as C2'. All alchemical transformations and their associated changes in the binding free energies are shown in **Figure 5**. The averaged values for each transformation in water and in the enzyme are given in the **Table 1**, while the values obtained for each of the five replicas are given in the Table S1.
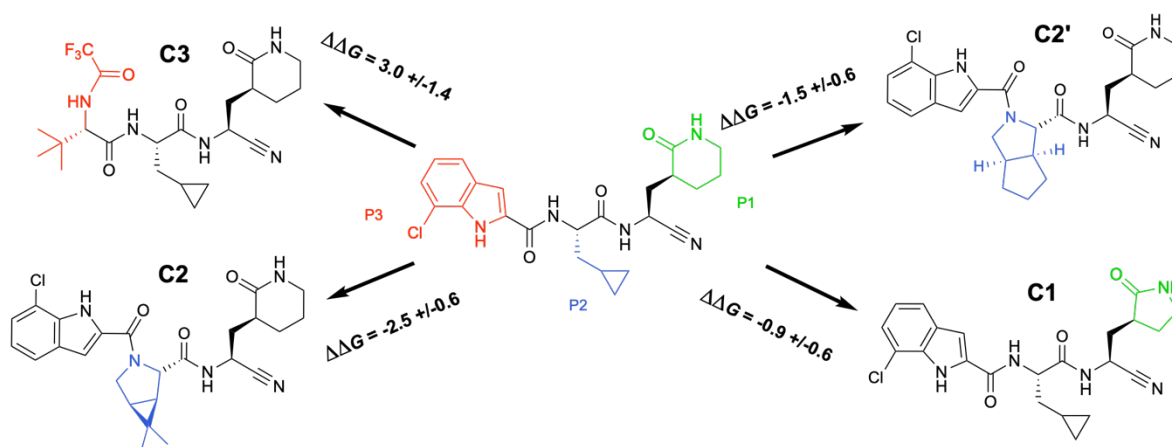

Figure 5. *Binding free energy changes related to the transformation of pomotrelvir Pi groups to the Pi groups in nirmatrelvir (C1 to C3) and the P2 group in UAWJ9-36-1, C2'.*

When the P1 side chain group of pomotrelvir was substituted with the P1 side chain group of nirmatrelvir, there was a small change of -0.9 ± 0.6 kcal·mol^{-1} in the binding free energy, in agreement with the observation made before that the NH group of nirmatrelvir γ-lactam ring interacts better with Glu166 than the δ-lactam ring of pomotrelvir. The presence of a γ-lactam ring at position P1 seems a better option than a δ-lactam ring for binding to the wild-type main protease.

More significant changes in the binding free energy were observed upon modification of the P2 group of pomotrelvir. A destabilising effect was observed during the transformation to C2 and C2' both in water and in the enzyme, see **Table 1**. The presence of a secondary amine in the pomotrelvir P2 group allows for hydrogen bonding interactions with water molecules in the solvent and with the Gln189 Oγ atom once the Michaelis complex is formed, as shown in Figure S5. In contrast, these interactions are not present in the case of the tertiary amine in the P2 group of nirmatrelvir (C2) or in the P2 group of UAWJ9-36-1 (C2'), see green and red curves in Figure S5. In water, for pomotrelvir it is observed a solvation shell of 2 water molecules around 3.5 Å of the amino group, while for C2 and C2' only one water molecule is solvating its tertiary amino group around 4 Å. For pomotrelvir in the enzyme, a weaker stabilization is made by the Gln189 Oγ atom, as shown in Figure S5 and thus the presence of a secondary amine disfavours the binding process. The overall transformation resulted in a notable improvement in binding energy, with an associated decrease of -2.5 ± 0.6 kcal·mol^{-1} in C2 and of -1.5 ± 0.6 kcal·mol^{-1} in C2'. This improvement in the binding free energy obtained upon the transformation of the secondary amine group in pomotrelvir to a tertiary amine group in C2 and C2', unable to act as proton donors seems, to be the key to the overall binding energy improvement. Missing this hydrogen bond interaction destabilizes more the inhibitor in water than in the active site, leading to a better binding free energy.

As discussed previously, the presence of a flexible side chain in the P2 group of pomotrelvir induces the frequent opening of the main protease active site due to the disruption of the hydrogen bond between residues Gln189 and Met49. When the P2 group of pomotrelvir is changed by a cyclized version, as in C2 or C2', we observe a noticeable increase in the fraction of conformations where this hydrogen bond is preserved. According to the results presented in table S2, obtained from three independent 1 μs simulations of the Michaelis complexes formed with pomotrelvir, C2 and C2', the Gln180-Met49 hydrogen bond is present in approximately 24% of configurations from simulations with pomotrelvir, while for the chimeric structures C2 and C2', this percentage is increased to 54% and 42%, respectively —values comparable to those observed for nirmatrelvir. We also monitored the hydrogen bon distance between the catalytic dyad (Cys145-His41) and the distance from the nucleophilic Sγ atom of Cys145 to the electrophilic carbon atom of the nitrile warheads, see Figure S6. The complexes formed with C2 and C2' display more frequently short distances compatible with the requirements of the chemical reaction leading to the formation of the covalent complex between the inhibitor and the enzyme. This analysis confirms that the presence of a flexible P2 side chain in pomotrelvir favours the loss of preorganization of the active site, disfavouring then the formation of the covalent complex.

Table 1. *Free energy changes for alchemical transformations of Pomotrelvir into C1, C2, C3, and C2' (see Figure 5) in aqueous and protein environments, along with $\Delta\Delta G_{binding}$ values. Estimated free energy values (kcal·mol^{-1}) are the result of five replicas and were obtained using Thermodynamic Integration. The errors correspond to the standard deviations.*

modification	ΔG_{water}	$\Delta G_{Protein}$	$\Delta\Delta G_{binding}$
C1	-0.1 ± 0.2	-1.0 ± 0.5	-0.9 ± 0.6
C2	12.4 ± 0.2	9.9 ± 0.6	-2.5 ± 0.6
C2'	11.2 ± 0.1	9.7 ± 0.6	-1.5 ± 0.6
C3	-36.7 ± 0.2	-33.7 ± 1.4	3.0 ± 1.4

Remarkably, the substitution of the rigid 7-chloroindole-2-carbonyl group at the P3 position of pomotrelvir with the *tert*-leucine and trifluoroacetyl groups in nirmatrelvir resulted in a destabilising effect on the binding free energy. This effect might be attributed to the presence of three fluorine atoms, one secondary amine group and two carbonyls in C3 that facilitate stronger interactions with both the solvent and the enzyme, unlike the P3 group of pomotrelvir, which only has one secondary amine group and one carbonyl group in this region. Note also that the larger flexibility of P3/P4 groups in nirmatrelvir can impose an entropic penalty for binding due to a restriction of their conformational freedom in the active site.

3.3. Formation of the covalent complex

Our investigation of the multidimensional free energy surface for the chemical reaction between SARS-CoV-2 main protease and pomotrelvir, using the ASM method, revealed a MFEP similar to that previously reported for nirmatrelvir.[9] The resultant free energy profile and the progression of the CVs throughout the reaction path are depicted in **Figure 6**a and **Figure 6**b respectively, while the one corresponding to nirmatrelvir is shown in Figure S7. According to the evolution of the CVs (see Figure 6b) the process starts with the activation of the catalytic dyad, with the proton transfer from Cys145 to His41 (see the evolution of the Sγ-Hγ and Nε-Hγ distances) , followed by the intervention of a water molecule that functions as a proton shuttle between His41 and the nitrile inhibitor group (see Hw-Ow, Hw-N, Nε-Hγ and Ow-Hγ distances) and the nucleophilic attack of Cys145 Sγ atom on the electrophilic carbon atom of the nitrile warhead (see the evolution of Sγ-C in Figure 6b).
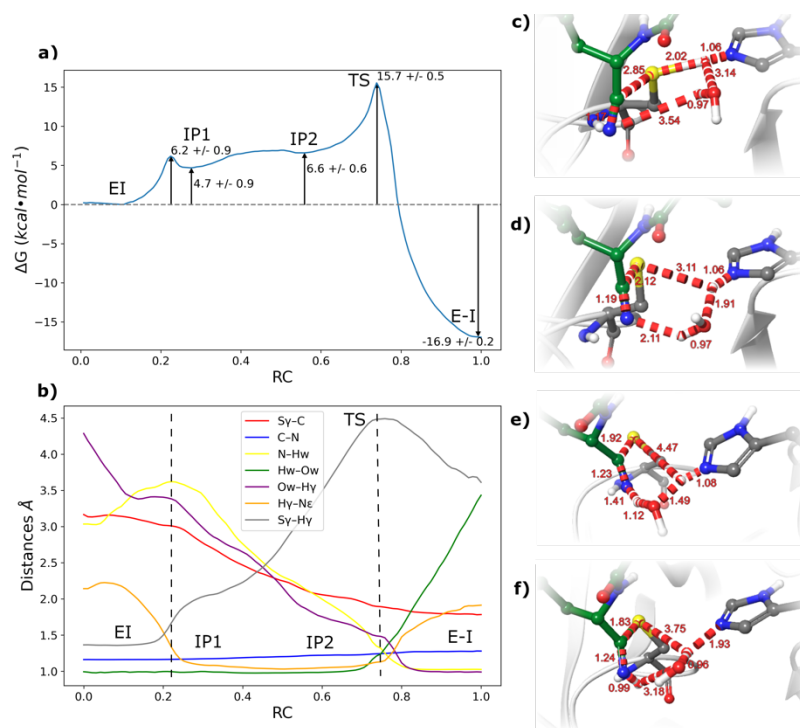
Figure 6. *Formation of the E-I complex between pomotrelvir and SARS-CoV-2 main protease. a) B3LYPD3/6-31+G*/MM free energy profile along the path-CV. b) Evolution of the CVs along the MFEP. The definition of the CVs is found in Figure 2, c) IP1 structure, d) IP2 structure, e) TS and f) product.*

A first energy barrier of 6.2 ± 0.9 kcal·mol^{-1} was identified. This barrier is associated with the proton transfer from the catalytic Cys145 to His41, to form the catalytic dyad in the ion pair (IP1) configuration. In the **Figure 6**b is observed that during the transfer of the Hγ atom from Cys145 Sγ atom to the Nϵ atom of His41, the oxygen atom of a water molecule becomes closer to the Hγ atom of Cys14, reducing the distance from 4.18 Å in the reactant state to 3.14 Å in the IP1 state, the ion pair formed after the proton transfer, that has a relative free energy with respect to the reactants of 4.7 ± 0.9 kcal·mol^{-1}. The geometry of IP1 is shown in **Figure 6**c. The ion pair rearranges into a higher-energy configuration IP2 (shown in Figure 6d) with a free energy of 6.6 ± 0.6 kcal·mol^{-1}. The observed increase in energy is associated to the separation of the catalytic dyad in such a way that the activated Cys145 becomes closer to the electrophilic carbon atom of the inhibitor (the Sγ-C reaches 2.12 Å). This process is assisted by the formation of the hydrogen bond between the hydrogen atom from water to the nitrogen atom in the nitrile group (Hw-C), and between the Hγ atom of Cys145 (now bonded to His41) and the oxygen atom of the water molecule (Ow-Hγ). At this point the distance of the triple C-N bond has been slightly lengthened from 1.15 Å in the reactant state to 1.19 Å.

From IP2, the reaction reaches the rate-determining Transition State (TS), with an activation free energy of 15.7 ± 0.5 kcal·mol^{-1} a value similar to the 18.2 kcal·mol^{-1} derived from the experimental rate constant for the reaction of the main protease with a peptidic substrate.[40] At this point the nucleophilic attack is almost completed, with the Sγ-C distance decreasing

to 1.89 Å. This stage is marked by the interchange of two protons: one proton moves from His41 to the water molecule, while the other one moves from the water to the nitrogen atom in the nitrile group of the inhibitor, as seen in **Figure 6**e. Significantly, the water molecule acting as a shuttle for the proton transfer is taking over the role usually played by the leaving amino group, see Figure S7, when the reaction takes place with its natural substrate.[32] The process culminates in the final product state where the water-assisted proton transfer is complete. This results in the formation of an exergonic thioimidate product (-16.9 ± 0.2 kcal·mol^{-1}), characterized by an Sγ-C distance of 1.83 Å, as shown in **Figure 6**f.

From the alchemical transformation study, it was observed that the chimeric structure with the best binding energy was C2. This makes it a good candidate for studying the formation of the covalent E-I complex using the same methodology applied to pomotrelvir. As expected, the mechanism obtained for C2 is very similar to that observed for pomotrelvir and nirmatrelvir (see Figure S7). No major changes are observed in the evolution of the collective variables during the chemical reaction with C2 when compared to pomotrelvir. The formation of the ion pair structure in presence of C2 is favoured with respect to pomotrelvir, with a free energy cost of only 2.3 ± 1.1 kcal·mol^{-1}, very similar to the value reported for nirmatrelvir.[9] For C2, the activation free energy barrier obtained for the formation of the covalent complex is 16.1 ± 0.7 kcal·mol^{-1}, very similar to the value computed for pomotrelvir, as seen in Figure S8a. While the reaction with pomotrelvir is slightly more exergonic than with C2, -16.9 ± 0.2 and -13.5 ± 0.1 kcal·mol^{-1} respectively, both values are clearly more negative than the value obtained for the reaction with nirmatrelvir, -9.5 kcal·mol^{-1}.[9] In this way, the reversibility of the inhibition with C2 seems not to be a matter of concern. In summary, the change of the cyclopropylmethyl group of pomotrelvir to the gem-dimethylcyclopropylproline present in C2 has three advantages: improves the binding free energy of the inhibitor, stabilizes the IP structure and the exergonicity to form the covalent E-I product is increased with respect to nirmatrelvir, although slightly worse than for pomotrelvir.

As discussed earlier, we observed a larger conformational flexibility of the active site in the Michaelis complex of the enzyme with pomotrelvir compared to nirmatrelvir. The high mobility is attributed to the non-cyclic nature of the P2 side chain present in pomotrelvir. Interestingly, this effect is reversed in C2, where the P2 group of pomotrelvir was replaced by the P2 group of nirmatrelvir. The comparison of the distribution of distances between the Cys145 Sγ and the His41 Nϵ atoms in the Michaelis complexes formed with pomotrelvir and C2 shows an increase in the population of reactive configurations in the latter (see Figure S6). The increase in the population of the reactive structures represents an additional advantage for the inclusion of cyclic P2 groups in the designing process of inhibitors for this enzyme. We can estimate the effect on the activation free energy by fitting the probability distributions presented in Figure S6 to a combination of gaussian distribution functions (see Table S3 for details). For pomotrelvir, the free energy cost required to exist in a reactive conformation (with a short Cys145-His41 hydrogen bond distance) is of about 1.1 kcal·mol^{-1}, whereas only 0.15 kcal·mol^{-1} is needed for C2. This effect on the preorganization of the

active site supports the use of other groups different to cyclopropylmethyl at the P2 position of nitrile inhibitors.

4. Conclusions

Using a combination of pure MM and hybrid QM/MM methodologies, the covalent inhibition of the SARS-CoV-2 main protease by pomotrelvir has been studied. We first analysed the formation of the noncovalent complex and as well as the contribution of each of its Pi fragments to the binding energy. We then determined the reaction mechanism for the formation of the covalent enzyme-inhibitor complex. This information can be helpful to formulate strategies to develop more potent inhibitors to fight COVID-19 infection.

Observations obtained from MD simulations suggest that the binding mode of pomotrelvir differs slightly from that of nirmatrelvir. The change in the hydrogen bonding pattern between pomotrelvir and Glu166 could negatively affect the stability of the P1 group in the S1 pocket of the wild type main protease. The γ-lactam ring present at the P1 position of nirmatrelvir appears to be, in principle, a better choice to occupy the P1 position than the δ-lactam ring of pomotrelvir, because the former establishes stronger interactions with Glu166. Nevertheless, this difference in the interactions established by than the δ-lactam and γ-lactam rings could turn into a potential advantage to inhibit the E166V mutant of the main protease with the former group.

Regarding the P2 group, the substitution of the cyclopropylmethyl moiety in pomotrelvir by a gem-dimethylcyclopropylproline group, as such present in nirmatrelvir, increases the binding energy of the inhibitor because the former establishes stronger hydrogen bond interaction in the solvent than in the enzyme through its secondary amine. The cyclisation of the side chain also favours the formation of reactive conformations leading to the covalent complex. Consequently, the gem-dimethylcyclopropylproline group is considered as a more suitable choice to occupy the P2 position than the cyclopropylmethyl group present in pomotrelvir.

Regarding the P3 group of pomotrelvir, the substitution of the 7-chloroindole-2-carbonyl group with *tert*-leucine and trifluoroacetyl groups, as those found at positions P3 and P4 of nirmatrelvir, decrease the binding free energy of the inhibitor. Both P3 groups of pomotrelvir and nirmatrelvir establish robust interactions with Glu166 side chain. As commented before, these interactions can be of interest for the design of new inhibitors, particularly if mutations in residue 166 are anticipated as a resistance mechanism of the virus against the treatments with nirmatrelvir.

As expected, the reaction mechanism for the formation of the covalent complex between the main protease and pomotrelvir is very similar to that described for nirmatrelvir. The

catalytic Cys145 must be activated by a proton transfer to His41 that leads to the formation of an ion pair, followed by a shuttle proton transfer mechanism through a water molecule from His41 to the nitrogen atom of the nitrile warhead and the nucleophilic attack of Cys145-Sγ atom to the electrophilic carbon atom. The activation free energy associated with the covalent inhibition is 15.7 kcal·mol^{-1}. As discussed above, the kinetic of the process could be also favoured by replacing the cyclopropylmethyl group of pomotrelvir with the gem-dimethylcyclopropylproline of nirmatrelvir. The Michaelis complex formed with the resulting inhibitor, C2, disturbs less the active site, facilitating the exploration of reactive conformations, while the activation free energy as determined from these conformations is almost identical (16.1 kcal·mol^{-1}). From the thermodynamic perspective, the exergonicity is decreased by 3.4 kcal·mol^{-1} when the enzyme reacts with C2 with respect to pomotrelvir, but is still 4.0 kcal·mol^{-1} more exergonic than for the covalent inhibition with nirmatrelvir.

As a summary, the combination of simulations performed in this work shows some important findings that can be useful to assist in the design of new inhibitors of SARS-CoV-2 main protease, particularly for the selection of the groups in P1 and P2 positions. We have shown that a δ-lactam ring is an adequate choice to be incorporated at the P1 position in the design of inhibitors designed against main protease, especially those variants presenting mutations at position 166. For the P2 position, tertiary amines are clearly preferred with respect to secondary amines. The possibility to act as a hydrogen bond donor seem to favour more the interaction with the solvent than with the protein, decreasing the affinity for the enzyme. In addition, flexible groups at P2 position disfavour the formation of the covalent complex because they can disrupt the preorganization of the active site, favouring the dynamical exploration of non-reactive conformations. Regarding the reaction mechanism to form the covalent enzyme-inhibitor complex, all the inhibitors analysed here, pomotrelvir, nirmatrelvir and C2, present a very similar mechanism and activation free energy. We hope that all these findings could be useful to fight present and future variants of SARS-CoV-2 virus.

5. Acknowledgements

References

(1) Bolon, B.; Haschek, W. M. The Exposome in Toxicologic Pathology. *Toxicol. Pathol.* **2020**, *48* (6), 718–720. https://doi.org/10.1177/0192623320912403.

(2) Owen, D. R.; Allerton, C. M. N.; Anderson, A. S.; Aschenbrenner, L.; Avery, M.; Berritt, S.; Boras, B.; Cardin, R. D.; Carlo, A.; Coffman, K. J.; Dantonio, A.; Di, L.; Eng, H.; Ferre, R.; Gajiwala, K. S.; Gibson, S. A.; Greasley, S. E.; Hurst, B. L.; Kadar, E. P.; Kalgutkar, A. S.; Lee, J. C.; Lee, J.; Liu, W.; Mason, S. W.; Noell, S.; Novak, J. J.; Obach, R. S.; Ogilvie, K.; Patel, N. C.; Pettersson, M.; Rai, D. K.; Reese, M. R.; Sammons, M. F.; Sathish, J. G.; Singh, R. S. P.; Steppan, C. M.; Stewart, A. E.; Tuttle, J. B.; Updyke, L.; Verhoest, P. R.; Wei, L.; Yang, Q.; Zhu, Y. An Oral SARS-CoV-2 Mpro Inhibitor Clinical Candidate for the Treatment of COVID-19. **2021**.

(3) Zhang, J.; Xiao, T.; Cai, Y.; Lavine, C. L.; Peng, H.; Zhu, H.; Anand, K.; Tong, P.; Gautam, A.; Mayer, M. L.; Jr, R. M. W.; Rits-Volloch, S.; Wesemann, D. R.; Yang, W.; Seaman, M. S.; Lu, J.; Chen, B. Membrane Fusion and Immune Evasion by the Spike Protein of SARS-CoV-2 Delta Variant. **2021**.

(4) Jochmans, D.; Liu, C.; Donckers, K.; Stoycheva, A.; Boland, S.; Stevens, S. K.; De Vita, C.; Vanmechelen, B.; Maes, P.; Trüeb, B.; Ebert, N.; Thiel, V.; De Jonghe, S.; Vangeel, L.; Bardiot, D.; Jekle, A.; Blatt, L. M.; Beigelman, L.; Symons, J. A.; Raboisson, P.; Chaltin, P.; Marchand, A.; Neyts, J.; Deval, J.; Vandyck, K. The Substitutions L50F, E166A, and L167F in SARS-CoV-2 3CLpro Are Selected by a Protease Inhibitor *In Vitro* and Confer Resistance To Nirmatrelvir. *mBio* **2023**, *14* (1), e02815-22. https://doi.org/10.1128/mbio.02815-22.

(5) Ramos-Guzmán, C. A.; Andjelkovic, M.; Zinovjev, K.; Ruiz-Pernía, J. J.; Tuñón, I. The Impact of SARS-CoV-2 3CL Protease Mutations on Nirmatrelvir Inhibitory Efficiency. Computational Insights into Potential Resistance Mechanisms. *Chem. Sci.* **2023**, *14* (10), 2686–2697. https://doi.org/10.1039/D2SC06584C.

(6) Zuckerman, N. S.; Bucris, E.; Keidar-Friedman, D.; Amsalem, M.; Brosh-Nissimov, T. Nirmatrelvir Resistance—de Novo E166V/L50V Mutations in an Immunocompromised Patient Treated With Prolonged Nirmatrelvir/Ritonavir Monotherapy Leading to Clinical and Virological Treatment Failure—a Case Report. *Clin. Infect. Dis.* **2023**, ciad494. https://doi.org/10.1093/cid/ciad494.

(7) Chan, H. T. H.; Oliveira, A. S. F.; Schofield, C. J.; Mulholland, A. J.; Duarte, F. Dynamical Nonequilibrium Molecular Dynamics Simulations Identify Allosteric Sites and Positions Associated with Drug Resistance in the SARS-CoV-2 Main Protease. *JACS Au* **2023**, *3* (6), 1767–1774. https://doi.org/10.1021/jacsau.3c00185.

(8) Tong, X.; Keung, W.; Arnold, L. D.; Stevens, L. J.; Pruijssers, A. J.; Kook, S.; Lopatin, U.; Denison, M.; Kwong, A. D. Evaluation of *in Vitro* Antiviral Activity of SARS-CoV-2 M [pro] Inhibitor Pomotrelvir and Cross-Resistance to Nirmatrelvir Resistance Substitutions. *Antimicrob. Agents Chemother.* **2023**, *67* (11), e00840-23. https://doi.org/10.1128/aac.00840-23.

(9)   Ramos-Guzmán, C. A.; Ruiz-Pernía, J. J.; Tuñón, I. Computational Simulations on the Binding and Reactivity of a Nitrile Inhibitor of the SARS-CoV-2 Main Protease. *Chem. Commun.* **2021**, *57* (72), 9096–9099. https://doi.org/10.1039/D1CC03953A.

(10)   Hilgenfeld, R. From SARS to MERS: Crystallographic Studies on Coronaviral Proteases Enable Antiviral Drug Design. *FEBS J.* **2014**, *281* (18), 4085–4096. https://doi.org/10.1111/febs.12936.

(11)   Zhu, M.; Fu, T.; You, M.; Cao, J.; Yang, H.; Chen, X.; Zhang, Q.; Xu, Y.; Jiang, X.; Zhang, L.; Su, H.; Zhang, Y.; Shen, J. Design, Synthesis and Biological Evaluation of Covalent Peptidomimetic 3CL Protease Inhibitors Containing Nitrile Moiety. *Bioorg. Med. Chem.* **2023**, *87*, 117316. https://doi.org/10.1016/j.bmc.2023.117316.

(12)   Ngo, S. T.; Nguyen, T. H.; Tung, N. T.; Mai, B. K. Insights into the Binding and Covalent Inhibition Mechanism of PF-07321332 to SARS-CoV-2 M ^{pro}. *RSC Adv.* **2022**, *12* (6), 3729–3737. https://doi.org/10.1039/D1RA08752E.

(13)   Pardes Biosciences, Inc. *PBI-0451 (Pomotrelvir) Phase 2 Study in Nonhospitalized Symptomatic Adults With COVID-19*. https://clinicaltrials.gov/study/NCT05543707 (accessed 2023-12-28).

(14)   Wang, J.; Wang, W.; Kollman, P. A.; Case, D. A. Automatic Atom Type and Bond Type Perception in Molecular Mechanical Calculations. *J. Mol. Graph. Model.* **2006**, *25* (2), 247–260. https://doi.org/10.1016/j.jmgm.2005.12.005.

(15)   Case, D. A.; Cheatham, T. E.; Darden, T.; Gohlke, H.; Luo, R.; Merz, K. M.; Onufriev, A.; Simmerling, C.; Wang, B.; Woods, R. J. The Amber Biomolecular Simulation Programs. *J. Comput. Chem.* **2005**, *26* (16), 1668–1688. https://doi.org/10.1002/jcc.20290.

(16)   Bayly, C. I.; Cieplak, P.; Cornell, W.; Kollman, P. A. A Well-Behaved Electrostatic Potential Based Method Using Charge Restraints for Deriving Atomic Charges: The RESP Model. *J. Phys. Chem.* **1993**, *97* (40), 10269–10280. https://doi.org/10.1021/j100142a004.

(17)   Maier, J. A.; Martinez, C.; Kasavajhala, K.; Wickstrom, L.; Hauser, K. E.; Simmerling, C. ff14SB: Improving the Accuracy of Protein Side Chain and Backbone Parameters from ff99SB. *J. Chem. Theory Comput.* **2015**, *11* (8), 3696–3713. https://doi.org/10.1021/acs.jctc.5b00255.

(18)   Berman, H.; Henrick, K.; Nakamura, H. Announcing the Worldwide Protein Data Bank. *Nat. Struct. Mol. Biol.* **2003**, *10* (12), 980–980. https://doi.org/10.1038/nsb1203-980.

(19)   Hoffman, R. L.; Kania, R. S.; Brothers, M. A.; Davies, J. F.; Ferre, R. A.; Gajiwala, K. S.; He, M.; Hogan, R. J.; Kozminski, K.; Li, L. Y.; Lockner, J. W.; Lou, J.; Marra, M. T.; Mitchell, L. J.; Murray, B. W.; Nieman, J. A.; Noell, S.; Planken, S. P.; Rowe, T.; Ryan, K.; Smith, G. J.; Solowiej, J. E.; Steppan, C. M.; Taggart, B. Discovery of Ketone-Based Covalent Inhibitors of Coronavirus 3CL Proteases for the Potential Therapeutic Treatment of COVID-19. *J. Med. Chem.* **2020**, *63* (21), 12725–12747. https://doi.org/10.1021/acs.jmedchem.0c01063.

(20)   Olsson, M. H. M.; Søndergaard, C. R.; Rostkowski, M.; Jensen, J. H. PROPKA3: Consistent Treatment of Internal and Surface Residues in Empirical pK_a Predictions. *J. Chem. Theory Comput.* **2011**, *7* (2), 525–537. https://doi.org/10.1021/ct100578z.

(21)   Ryckaert, J.-P.; Ciccotti, G.; Berendsen, H. J. C. Numerical Integration of the Cartesian Equations of Motion of a System with Constraints: Molecular Dynamics of n-Alkanes. *J. Comput. Phys.* **1977**, *23* (3), 327–341. https://doi.org/10.1016/0021-9991(77)90098-5.

(22)   Darden, T.; York, D.; Pedersen, L. Particle Mesh Ewald: An $N \cdot \log(N)$ Method for Ewald Sums in Large Systems. *J. Chem. Phys.* **1993**, *98* (12), 10089–10092. https://doi.org/10.1063/1.464397.

(23)   Essmann, U.; Perera, L.; Berkowitz, M. L.; Darden, T.; Lee, H.; Pedersen, L. G. A Smooth Particle Mesh Ewald Method. *J. Chem. Phys.* **1995**, *103* (19), 8577–8593. https://doi.org/10.1063/1.470117.

(24)   Le Grand, S.; Götz, A. W.; Walker, R. C. SPFP: Speed without Compromise—A Mixed Precision Model for GPU Accelerated Molecular Dynamics Simulations. *Comput. Phys. Commun.* **2013**, *184* (2), 374–380. https://doi.org/10.1016/j.cpc.2012.09.022.

(25)   Salomon-Ferrer, R.; Götz, A. W.; Poole, D.; Le Grand, S.; Walker, R. C. Routine Microsecond Molecular Dynamics Simulations with AMBER on GPUs. 2. Explicit Solvent Particle Mesh Ewald. *J. Chem. Theory Comput.* **2013**, *9* (9), 3878–3888. https://doi.org/10.1021/ct400314y.

(26)   Zinovjev, K.; Tuñón, I. Adaptive Finite Temperature String Method in Collective Variables. *J. Phys. Chem. A* **2017**, *121* (51), 9764–9772. https://doi.org/10.1021/acs.jpca.7b10842.

(27)   Zinovjev, K.; Ruiz-Pernía, J. J., Tuñón I. Toward an Automatic Determination of Enzymatic Reaction Mechanisms and Their Activation Free Energies. *J. Chem. Theory Comput.* **2013**, *9* (8), 3740–3749. https://doi.org/10.1021/ct400153r.

(28)   Kumar, S.; Rosenberg, J. M.; Bouzida, D.; Swendsen, R. H.; Kollman, P. A. THE Weighted Histogram Analysis Method for Free-Energy Calculations on Biomolecules. I. The Method. *J. Comput. Chem.* **1992**, *13* (8), 1011–1021. https://doi.org/10.1002/jcc.540130812.

(29)   Lee, C.; Yang, W.; Parr, R. G. Development of the Colle-Salvetti Correlation-Energy Formula into a Functional of the Electron Density. *Phys. Rev. B* **1988**, *37* (2), 785–789. https://doi.org/10.1103/PhysRevB.37.785.

(30)   Becke, A. D. Density-Functional Thermochemistry. III. The Role of Exact Exchange. *J. Chem. Phys.* **1993**, *98* (7), 5648–5652. https://doi.org/10.1063/1.464913.

(31)   Grimme, S.; Antony, J.; Ehrlich, S.; Krieg, H. A Consistent and Accurate *Ab Initio* Parametrization of Density Functional Dispersion Correction (DFT-D) for the 94 Elements H-Pu. *J. Chem. Phys.* **2010**, *132* (15), 154104. https://doi.org/10.1063/1.3382344.

(32)   Ramos-Guzmán, C. A.; Ruiz-Pernía, J. J.; Tuñón, I. Unraveling the SARS-CoV-2 Main Protease Mechanism Using Multiscale Methods. *ACS Catal.* **2020**, *10* (21), 12544–12554. https://doi.org/10.1021/acscatal.0c03420.

(33)   Ramos-Guzmán, C. A.; Ruiz-Pernía, J. J.; Tuñón, I. Multiscale Simulations of SARS-CoV-2 3CL Protease Inhibition with Aldehyde Derivatives. Role of Protein and Inhibitor Conformational Changes in the Reaction Mechanism. *ACS Catal.* **2021**, *11* (7), 4157–4168. https://doi.org/10.1021/acscatal.0c05522.

(34)   Ramos-Guzmán, C. A.; Ruiz-Pernía, J. J.; Tuñón, I. A Microscopic Description of SARS-CoV-2 Main Protease Inhibition with Michael Acceptors. Strategies for Improving Inhibitor Design. *Chem. Sci.* **2021**, *12* (10), 3489–3496. https://doi.org/10.1039/D0SC04978F.

(35)   Paasche, A.; Schirmeister, T.; Engels, B. Benchmark Study for the Cysteine–Histidine Proton Transfer Reaction in a Protein Environment: Gas Phase, COSMO, QM/MM Approaches. *J. Chem. Theory Comput.* **2013**, *9* (3), 1765–1777. https://doi.org/10.1021/ct301082y.

(36)   Zinovjev, K. *String-Amber*. GitHub repository. https://github.com/kzinovjev/string-amber (accessed 2020-06-24).

(37)   Frisch, M. J.; Trucks, G. W.; Schlegel, H., B.; Scuseria, G. E.; Robb, M. A.; Cheeseman, J. R.; Scalmani, G.; Barone, V.; Petersson, G. A.; Nakatsuji, H.; Li, X.; Caricato, M.; Marenich, A. V.; Bloino, J.; Janesko, B. G.; Gomperts, R.; Mennucci, B.; Hratchian, H. P.; Ortiz, J. V.; Izmaylov, A. F.; Sonnenberg, J.; Williams-Young, D.; Ding, F.; Lipparini, F.; Egidi, F.; Goings, J.; Peng, B.; Petrone, A.; Henderson, T.; Ranasinghe, D.; Zakrzewski, V. G.; Gao, J.; Rega, N.; Zheng, G.; Liang, W.; Hada, M.; Ehara, M.; Toyota, K.; Fukuda, R.; Hasegawa, J.; Ishida, M.; Nakajima, T.; Honda, Y.; Kitao, O.; Nakai, H.; Vreven, T.; Throssell, K.; Montgomery, J. A.; Peralta, J. E.; Ogliaro, F.; Bearpark, M. J.; Heyd, J. J.; Brothers, E. N.; Kudin, K. N.; Staroverov, V. N.; Keith, T. A.; Kobayashi, R.; Normand, J.; Raghavachari, K.; Rendell, A. P.; Burant, J. C.; Iyengar, S. S.; Tomasi, J.; Cossi, M.; Millam, J. M.; Klene, M.; Adamo, C.; Cammi, R.; Ochterski, J. W.; Martin, R. L.; Morokuma, K.; Farkas, O.; Foresman, J. B.; Fox, D. J. Gaussian 16, Revision C.01. **2016**.

(38)   He, X.; Liu, S.; Lee, T.-S.; Ji, B.; Man, V. H.; York, D. M.; Wang, J. Fast, Accurate, and Reliable Protocols for Routine Calculations of Protein–Ligand Binding Affinities in Drug Design Projects Using AMBER GPU-TI with ff14SB/GAFF. *ACS Omega* **2020**, *5* (9), 4611–4619. https://doi.org/10.1021/acsomega.9b04233.

(39)   Xia, Z.; Sacco, M.; Hu, Y.; Ma, C.; Meng, X.; Zhang, F.; Szeto, T.; Xiang, Y.; Chen, Y.; Wang, J. Rational Design of Hybrid SARS-CoV-2 Main Protease Inhibitors Guided by the Superimposed Cocrystal Structures with the Peptidomimetic Inhibitors GC-376, Telaprevir, and Boceprevir. *ACS Pharmacol. Transl. Sci.* **2021**, *4* (4), 1408–1421. https://doi.org/10.1021/acsptsci.1c00099.

(40)   Ullrich, S.; Ekanayake, K. B.; Otting, G.; Nitsche, C. Main Protease Mutants of SARS-CoV-2 Variants Remain Susceptible to Nirmatrelvir. *Bioorg. Med. Chem. Lett.* **2022**, *62*, 128629. https://doi.org/10.1016/j.bmcl.2022.128629.